

Evaluation of Center-Line Extraction Algorithms in Quantitative Coronary Angiography

H. Greenspan*, M. Laifenfeld, S. Einav, and O. Barnea, *Senior Member, IEEE*

Abstract—Objective testing of centerline extraction accuracy in quantitative coronary angiography (QCA) algorithms is a very difficult task. Standard tools for this task are not yet available. We present a simulation tool that generates synthetic angiographic images of a single coronary artery with predetermined centerline and diameter function. This simulation tool was used creating a library of images for the objective comparison and evaluation of QCA algorithms. This technique also provides the means for understanding the relationship between the algorithms' performance and limitations and the vessel's geometrical parameters. In this paper, two algorithms are evaluated and the results are presented.

Index Terms—Centerline estimation, coronary geometrical complexity, lumen centerline detection, performance evaluation, QCA, simulation tool.

I. INTRODUCTION

QUANTITATIVE coronary angiography (QCA) has been developed to apply the speed and precision of computer processing to the analysis of coronary disease. Motivated by shortcomings of visual assessment of coronary angiograms [1], [2], full and semi-automated methods were sought to estimate the geometrical vessel parameters out of an individual angiogram (e.g., [3] and [4]). An important step in QCA and essential geometrical parameter for clinical purposes is the vessel's centerline. Vessel centerlines have been used in computing edge gradients and searching for border positions [5]–[8], to derive video-densitometric profiles [5], for measurement of vessel diameters [5], [6], [9], for calculation of lesion symmetry [4], and as the basis for three-dimensional (3-D) reconstruction of vessel segments or of the entire arterial tree [9]–[12].

Today, the most common approach to determine coronary lumen centerline is based on manual tracing of the entire centerline or manual identification of several centerline points and interpolation to produce a continuous centerline (e.g., [5] and [7]). The visual approach is limited by high intraobserver and interobserver variability [1], [2]. It has been shown that manual centerline identification results in vessel orientation errors of

5° – 10° in moderately curved vessels and up to 15° in more irregularly shaped vessels [3]. A manually specified starting estimate for the centerline may be used to identify the coronary borders followed by calculation of the lumen centerline as a line midway between the left and right coronary borders [3], [4]. In [13], each cross section of the artery segment of interest is separately processed for detecting its border points. In [14], a robust method of coronary border detection is proposed. This method is based on simultaneous identification of both vessel's borders. The lumen centerline is extracted as the midline between the simultaneously extracted borders [15].

The need for an operator to enter centerline points can be minimized and the reproducibility could be improved by performing a search to determine a maximum brightness path through the vessel segment of interest, using graph searching techniques on node brightness values [8], [15]. A number of centerline detection algorithms are based on vessel tracking, preserving continuity constraints of vessel position, curvature, diameter, and density [5], [6], [16]. Other approaches to coronary lumen centerline detection utilize mathematical morphology [17] or active contour models or snakes [8], [18]. Active contour models are suitable for analysis of angiographic *sequences* where the vessel centerline is manually or semi-automatically identified in the first frame. The snake algorithm tracks the vessel centerline in subsequent frames.

In arterial tree extraction techniques, the artery network *skeleton* is extracted using recursive sequential tracking, and the artery borders are extracted using directional resampling of the angiogram based on the extracted skeleton [17], [19]. Skeleton algorithms are based on minimum distance fields. The accuracy of the skeleton affects the artery border extraction stage. In [20], each artery segment is analyzed for skeleton and border extraction, using morphological tools of homotopy modification and watershed transform. In [21], 3-D skeleton and centerline generation is presented based on minimum distance fields. The extension to volumetric objects is presented in [22]. The skeletons are interpreted as connected centerlines, consisting of sequences of medial points of consecutive clusters. The centerlines are initially extracted as paths of voxels, followed by medial point replacement, refinement, smoothness, and connection operations.

In most of the algorithms mentioned, difficulties are introduced if the quality of the image is poor, and with an increased difficulty in the vessel geometry. Despite its significance, little has been done in examining the estimated centerline accuracy, and in particular, the relationship of performance to vessel geometry. The validation methodology in most QCA algorithms is based on comparing results with specialists' assessments or

Manuscript received February 15, 2000; revised June 18, 2001. This work was supported by the Elizabeth and Nicholas Slezak Super-center for Cardiac research and Medical Engineering. The work of H. Greenspan was supported by the Israeli Ministry of Science under the Eshkol Grant. The Associate Editor responsible for coordinating the review of this paper and recommending its publication was J. Liang. *Asterisk indicates corresponding author.*

*H. Greenspan is with the Department of Biomedical Engineering, Faculty of Engineering, Tel-Aviv University, Tel-Aviv 69978, Israel (e-mail: hayit@eng.tau.ac.il).

M. Laifenfeld, S. Einav, and O. Barnea are with the Department of Biomedical Engineering, Faculty of Engineering, Tel-Aviv University, Tel-Aviv 69978, Israel.

Publisher Item Identifier S 0278-0062(01)08664-5.

generating phantoms of known parameters (e.g., [8], [12], and [23]). Both methods are far from ideal. The first suffers from a lack of an objective criteria as well as inter-observer variability. The second requires a full imaging system to test the software and does not provide standard results. In [23], we find an initial attempt at assessing the accuracy of the vessel's estimated centerline. Indexes expressing the positional and orientation similarities of two centerlines are proposed. The results presented in [23] use the indexes to compare between centerlines, with the validation methodology based on human experts' defined ground truth and a comparison across additional computational methods, with no ground truth.

This paper describes a method that was developed to provide an objective accuracy measure for evaluating centerline extraction algorithms. The method compares estimated results with *a priori* data that was used to generate the centerline. Images of blood vessels with known geometry and centerline were synthesized. Means for an objective comparison of different QCA algorithms are presented, as well as a means for the evaluation of a specific QCA algorithm performance under different geometrical parameters of the vessel. A synthetic vessel-generation tool is shown and applied in the evaluation and comparison of two well-known centerline estimation algorithms.

A formulation of the geometric model for the coronary angiographic image is presented in Section II. An extension of the geometrical model to intensity information is discussed. In Section III, the synthetic vessel-generation tool is introduced. This paper focuses on utilizing the tool in assessing and comparing two centerline estimation algorithms. The algorithms are defined in Section IV and the performance evaluation study is presented in Section V. A discussion of the results is conducted in Section VI.

II. MODELING THE CORONARY ANGIOGRAPHIC IMAGE

We start with formulating a two-dimensional (2-D) geometrical representation of the vessel's projection. A vessel projection intensity model will be introduced in Section II-B.

A. Generating a 2-D Geometrical Model

In this section, we describe the steps entailed in the generation of a 2-D geometrical model for the vessel. In the following description, several basic assumptions and terminology are used: We consider the projection of a vessel, in terms of its borders, as two 2-D nonintersecting curves in the X - Y plane. A *centerline* is a curve such that any line normal to it (profile) intersects both borders at equal distances from that curve. That distance is the vessel's radius. The *radius function* (or *diameter function*), D , is the vessel's radius (diameter) as a function of the centerline's arc length (we will be using the two terms interchangeably).

The two main components of the vessel's geometrical model are the centerline and the borders of the vessel. The vessel borders can be generated using the vessel's centerline and radius function, as follows: generate the centerline; compute the normals (profiles) to the curve; compute the points on the profiles whose distance from the centerline correspond to the appropriate value of the radius function; Interpolate the resulting set of points to produce two smooth border curves.

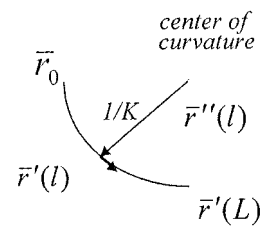


Fig. 1. Center of curvature and curvature radius.

1) *Generating the Vessel's Centerline*: We start with defining the centerline to be a curve with a piecewise constant curvature function. The centerline is generated from segments of different length and constant curvature. Curves with piecewise constant curvature are continuous and second degree smooth. These properties are reasonable when considering blood vessels' centerlines.

A 2-D curve is fully defined by its curvature function and a set of initial conditions. As the origin of the angiogram can be moved or rotated, with no loss of generality, the initial conditions will be fixed for all vessels' centerlines. The parametric equation of a curve may be written as $\bar{r} = \bar{r}(l)$ where \bar{r} represents a position vector and l is the curve *arc length*. The curve's *tangent*, \hat{t} , and *principal normal*, \hat{n} , are defined as: $\hat{t} = d\bar{r}/dl$, $\hat{n} = (d^2\bar{r}/dl^2)/|d^2\bar{r}/dl^2|$, respectively, where $||$ represents the modulus operator.

The *curvature* of a curve, K , is defined as the modulus of the second derivative of \bar{r} with respect to l : $d^2\bar{r}/dl^2 = K\hat{n}$. Curves of constant curvature, K , form semi-circles of radius $1/K$, as shown in Fig. 1. The center of this circle and its radius are called the *center of curvature* and the *curvature radius*, respectively. Semi circles in two dimensions may be written in vector form as

$$\begin{aligned}\bar{r}(l) &= \bar{r}_0 + \frac{1}{K}\bar{r}'_0 \cdot \phi_1; \\ \phi_1 &= \begin{bmatrix} \sin(lK) & 1 - \cos(lK) \\ \cos(lK) - 1 & \sin(lK) \end{bmatrix} \\ \bar{r}'(l) &= \bar{r}'_0 \cdot \phi_2; \\ \phi_2 &= \begin{bmatrix} \cos(lK) & \sin(lK) \\ -\sin(lK) & \cos(lK) \end{bmatrix}.\end{aligned}\quad (1)$$

In (1), $0 < l < L$ is the arc length parameter and L is the total curve length. The initial position of the semi-circle is \bar{r}_0 with the tangent represented by \bar{r}'_0 . A second semi-circle may be concatenated to the first by using the initial conditions $\bar{r}(L)$, $\bar{r}'(L)$ in the initial curve definition. A 2-D curve representing the vessel's centerline is generated by concatenating semi-circles of different lengths and curvatures.

2) *Generating the 2-D Vessel's Profiles*: We next compute the profiles, as the normals to points on the centerline. The direction vector of a given profile is perpendicular to the curve tangent at that point. Rotating the tangent by 90° results in the *profile direction vector* (dependent on location along the curve arclength, l)

$$\hat{n}(l) = (-\sin(lK) - \cos(lK), \cos(lK) - \sin(lK)). \quad (2)$$

TABLE I
PARAMETERS OF THE SVG SYNTHETIC VESSEL IMAGE DATABASE

	1	2	3	4	5	6	7	8	9	10	11	12	13	14	15	16	17	18	19
Taper [X1000]	-	-	-	-	-	-	-	-	-	-	-	-	1.45	1.45	1.45	1.45	1.45	1.45	1.45
Stenosis [%]	30	32	35	38	53	56	60	65	80	85	90	95	30	35	53	56	85	90	95
Curv[x1000]	-	-	-	-	-	-	-	-	-	-	-	-	-	-	-	-	-	-	-
θ [x100rad]	-	-	-	-	-	-	-	-	-	-	-	-	-	-	-	-	-	-	-

(a)

	20	21	22	23	24	25	26	27	28	29	30	31	32
Taper [X1000]	0.8	0.8	0.8	0.8	0.8	0.8	0.8	0.8	0.8	0.8	0.8	0.8	0.8
Stenosis [%]	-	-	-	-	-	-	-	-	-	-	-	-	-
Curv[x1000]	3	3	3	3	6	6	6	6	6	9	9	9	9
θ [x100rad]	44	94	130	159	45	91	125	156	189	45	93	125	158

(b)

	33	34	35	36	37	38	39	40	41	42	43
Taper [X1000]	0.8	0.8	0.8	0.8	0.8	0.8	0.8	0.8	0.8	0.8	0.8
Stenosis [%]	-	-	-	-	-	-	-	-	-	-	-
Curv[x1000]	12	12	12	12	12	12	15	15	15	15	15
θ [x100rad]	189	45	94	126	157	189	45	92	123	157	188

(c)

	44	45	46	47	48	49	50	51	52
Taper[X1000]	0.8	0.8	0.8	0.8	0.8	0.8	0.8	0.8	0.8
Stenosis [%]	35	56	85	35	56	85	35	56	85
Curv[x1000]	3	3	3	9	9	9	15	15	15
θ [x100rad]	94	94	94	125	125	125	157	157	157

(d)

	53	54	55	56	57	58	59	60	61
Taper[X1000]	1	1	1	1	1	1	1	1	1
Stenosis [%]	70.7	80	77.5	55.7	56.1	52.8	92.2	90.1	90.1
Curv[x1000]	*	*	*	*	*	*	*	*	*
θ [x100rad]	*	*	*	*	*	*	*	*	*

The *Taper* parameter refers to parameter a ; the *Stenosis* parameter is $1/\sigma$ (%); *Curvature* is the parameter K ; θ is the length of the segment in radians. Four vessel geometry groups are studied: (a) vessels with zero curvature; zero taper or medium taper value; with stenosis; (b) vessels with varying curvature (knee-type); no stenosis; (c) vessels with curvature; with stenosis; and (d) multiple-segment vessels and asymmetric stenosis vessels. Parameters of the multiple-segments (*) are listed in Table II

3) *Generating the Vessel's Radius Function:* The *radius function* is constructed as a combination of an exponentially decaying function, simulating a natural narrowing (tapering) of the vessel as a function of its length, along with a Gaussian

TABLE II
PARAMETERS OF THE SVG SYNTHETIC VESSEL IMAGE DATABASE

Image	Curv [x1000]					θ [x100rad]						Curv [x1000]					θ [x100rad]				
Segment	1	2	3	4	5	1	2	3	4	5	Segment	1	2	3	4	5	1	2	3	4	5
Image											Image										
53	0	-4.2	9.6	4.2	0	0	42	96	42	0	58	0	-1.8	7.8	-1.9	0	0	22	47	21	0
54	4.5	-2.1	13.1	0.6	4.7	45	21	97	7	47	59	0	-4.7	34.9	-4.2	0	0	46	143	66	0
55	-2.4	-5.6	11.1	-5.7	-2.5	24	49	64	86	25	60	4.5	-1.9	20	-2.4	3.6	45	21	133	22	44
56	-2.4	-5.6	5	-5.7	-2.5	24	49	29	86	25	61	-5.5	-12.6	19.5	-12.5	-2.5	67	66	102	111	45
57	3.9	-4	9.1	-0.6	4.7	39	4	67	7	47											

Vessels #53–#61 are comprised of five segments. The table lists the curvatures and lengths of each of the five segments/vessel.

function simulating a stenosis

$$\begin{aligned}
 D(l) &= f(l|D_0, a, \sigma, \mu) = D_0 e^{-al} \\
 &\quad - \frac{c}{\sigma} \exp\left(-\frac{\pi(l-\mu)^2}{(\sigma c)^2}\right); \\
 c &= D_0 e^{-a\mu}.
 \end{aligned} \tag{3}$$

D_0 and a are coefficients that represent the natural narrowing of the vessel. The vessel taper is a and D_0 is an initial diameter constant, held constant in all runs. The Gaussian function parameters are μ and σ . It can be seen that for an infinite σ the second term vanishes, simulating a no-stenosis situation. At the point of stenosis, $l = \mu$, setting $\sigma = 1$ results in the second term equaling c , simulating a 100% stenosis. The vessel's stenosis is, therefore, proportional to σ

$$\text{stenosis} \propto \frac{1}{\sigma}. \tag{4}$$

Using the vessel's radius function (3) with (1) and (2), the border points can be computed as follows:

$$B(l) = \bar{r}(l) \pm D(l)\hat{n}(l). \tag{5}$$

The set of parameters required for synthesizing vessels, as indicated by (5), include centerline parameters of the centerline's total curve length (L) and the desired curvature (K), as well as the radius function parameters of the taper (a) and stenosis (μ and σ), and the initial radius D_0 . This parameter set is used in the synthetic vessel-generating tool (Section III). Fig. 12 and Tables I and II show a set of synthetic vessels with the corresponding parameters.

B. The Vessel's Projection Intensity Model

In this paper, we focus mainly on the vessel's geometrical model, as described above. The geometrical model may be extended to include intensity information in the simulated image. An angiographic image is produced by the reaction of a sensitive film to intercepting X-ray beams passing through the patient's body. The intensity of the received X-ray beam, $I(x, y)$,

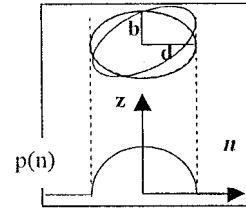


Fig. 2. Ellipse and its linear integral projection.

is a linear integral of the attenuation coefficient of the matter it encounters on its way. $I(x, y)$ forms a 2-D image that will be referred to as the vessel's intensity image. We describe next a model for the angiographic image based on the assumption of an elliptical vessel cross section [13]. Several steps are involved in modeling the intensity image. We start with a model of the vessel's cross section. Using the geometrical definition of the centerline (as in Section II-A), an elliptical cross section that is perpendicular to the centerline is assumed. The ellipse axes (major and minor) of the cross section are taken as continuous and slow-varying functions of the centerline's arc-length [as defined in (3)]. These assumptions result in a geometrical object usually referred to as "generalized cone" or "cylinder."¹

In modeling the vessel's cross section, consider a point, l_j , along the simulated vessel arclength, and denote by d and n the vessel's radius and the vessel's radius direction at that point, respectively: $d = D(l_j)$; $n = \hat{n}(l_j)$. Let z denote the cross-section axis (note that z is perpendicular to the t - n plane as shown in Fig. 2). An ellipse in the n - z plane is mathematically defined as: $n^2/d^2 + z^2/b^2 = 1$, where d and b represent the major and minor axes, respectively.

The ellipse intensity projection along the z axis, $p(n)$, is given by

$$p(n) = \frac{2b}{d} \sqrt{d^2 - n^2}, \quad |n| \leq d. \tag{6}$$

¹Note that such a definition may be suitable for healthy vessels, yet may deviate significantly from obstructed vessels in which the shape of the cross section at the obstruction is irregular.

Equation (6) represents the projection of a family of ellipses of similar area, that answer to: $b^2 \sin^2 \theta + d^2 \cos^2 \theta = \text{Const}$ [24]. Thus, it is sufficient to simulate a vessel with no rotation (with major and minor axis of the ellipse representing the vessel's cross section within the projection plane), without loss of generality. Note that b , the ellipse axis along the z direction, is a function of l , the vessel's arclength. Taking into account the intensity attenuation due to the nonuniform distribution of the contrast substance, b may be represented as: $b(l) = Bi \exp(-a_i l)$, where Bi and a_i are parameters controlling the vessel's contrast with respect to the background and the contrast attenuation coefficient, respectively.

With the vessel's intensity image defined as above, we continue with a model for the background contribution, $Bg(n)$. The objects constructing the background, namely bones and muscle, are much larger than the blood vessel, thus the intensity of their projection is slowly varying in space. Such a behavior is often modeled via a low order polynomial [25]. We consider the contribution of the background to the intensity image $I(x, y)$ in terms of the coordinates (x, y) and the polynomial's order, N

$$Bg(x, y) = \sum_{i=0}^N \alpha_i x^i + \beta_i y^i. \quad (7)$$

Note that at any direction in the x - y plane the intensity is a polynomial function of at most degree $N + 1$: Let $x = x_0 + ndx$, $y = y_0 + ndy$ be the parametric equations of the straight line representing the profile's direction. The intensity along this profile will be

$$\begin{aligned} Bg(n) &= \sum_{i=0}^N \alpha_i (x_0 + ndx)^i + \beta_i (y_0 + ndy)^i \\ &= \sum_{i=0}^N \sum_{l=0}^i \gamma_{il} n^i = \sum_{s=0}^N \lambda_s n^s. \end{aligned}$$

The following steps in modeling the intensity image account for the distortions produced by the imaging system, such as resolution limitations and additive noise. Blur is simulated by a convolution with a Gaussian spread function, $g(x, y)$. Noise, $\text{noise}(x, y)$ is added to the acquired image by an additive white Gaussian noise with zero mean and variance σ_N [24].

The final model of the intensity image is comprised of the above-described steps. Equation (6) determines the projected intensity profiles perpendicular to the vessel's centerline. Background contribution is added as defined in (7). Applying blur, $g(x, y)$, and adding noise, $\text{noise}(x, y)$ we produce the desired simulated intensity image map, $I(x, y)$, as

$$I(x, y) = (p(x, y) + Bg(x, y)) * g(x, y) + \text{noise}(x, y). \quad (8)$$

Note that the models defined in (5) and (8), are defined in the continuous domain. A quantization step onto the 2-D pixel grid is needed in actual implementation. In the implementation of the intensity model, the 2-D borders need to be sampled at discrete (application defined) intervals, to extract the intensity profiling at relevant increments of the vessel.

In the following evaluation process, we focus on the geometrical model (5) and the centerline definition in particular.

III. THE SYNTHETIC VESSEL-GENERATION SIMULATION TOOL

Fig. 3 shows the user interface of the synthetic vessel generator (SVG) tool. Fig. 3(a) shows an example of generating a geometrical model (2-D binary form). The vessel with the added intensity image is shown in Fig. 3(b). In the example presented, the 2-D synthetic vessel's centerline is constructed of five constant curvature segments with the following parameters (left to right): $K_1 = -0.006$, $L_1 = 120$; $K_2 = -0.012$, $L_2 = 60$; $K_3 = 0.02$, $L_3 = 50$; $K_4 = 0.012$, $L_4 = 90$; $K_5 = -0.002$; $L_5 = 175$. Here, each segment's length, L_i , is measured in pixels, and the negative curvature segments represent a tangent that is directed counter clockwise. The segment's total arclength is formulated in radians: $\theta_i = K_i L_i$ [rad]. The vessel's borders are constructed using a radius/diameter function that is shown in the upper right corner of the screen. The user-defined parameters are: a , the natural taper of the vessel (may accept any real value); s (sigma), the severity of the stenosis [ranging from one (100% stenosis) to infinity (no stenosis)]; r_0 , the initial vessel radius (in pixels); and μ , the stenosis location along the centerline arclength (in pixels).

Intensity information is presented in the bottom screen. User-defined parameters include the additive white Gaussian noise variance and mean values, the variance of the Gaussian blur function, the background x and y polynomials and the parameters B_i and a_i that control the profiles' intensity information (z direction).

A set of synthetic vessel images was created and analyzed using the simulation tool. Fig. 12 shows a selection of 61 synthetic vessels with the corresponding parameters listed in Tables I and II. Four main vessel geometries were studied.

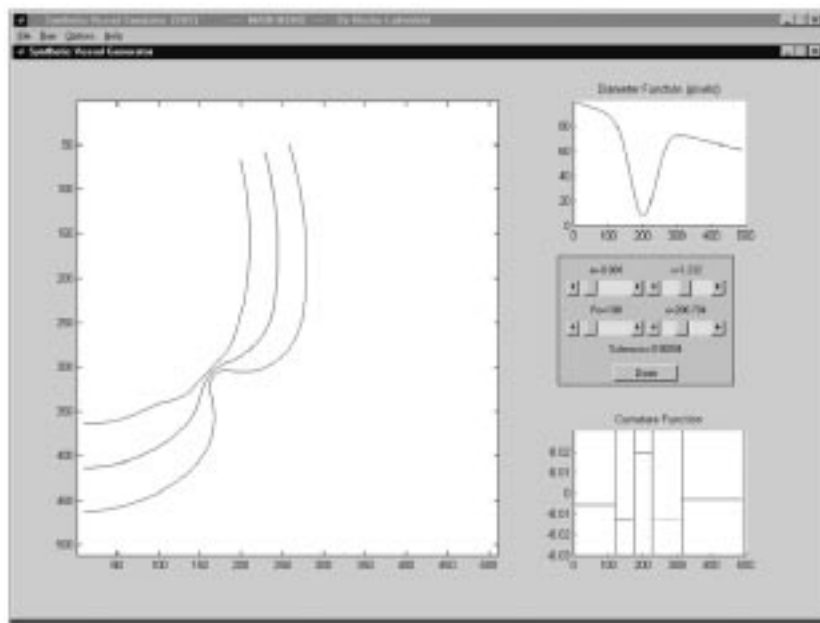
- 1) vessels with zero curvature; zero taper or medium taper value; with stenosis (vessels #1-#19).
- 2) vessels with varying curvature (knee-type); no stenosis (vessels #20-#43).
- 3) vessels with curvature; with stenosis (vessels #44-#52).
- 4) multiple-segment vessels and asymmetric stenosis vessels (vessels #53-#61).

IV. GEOMETRICAL ALGORITHMS FOR CENTERLINE ESTIMATION

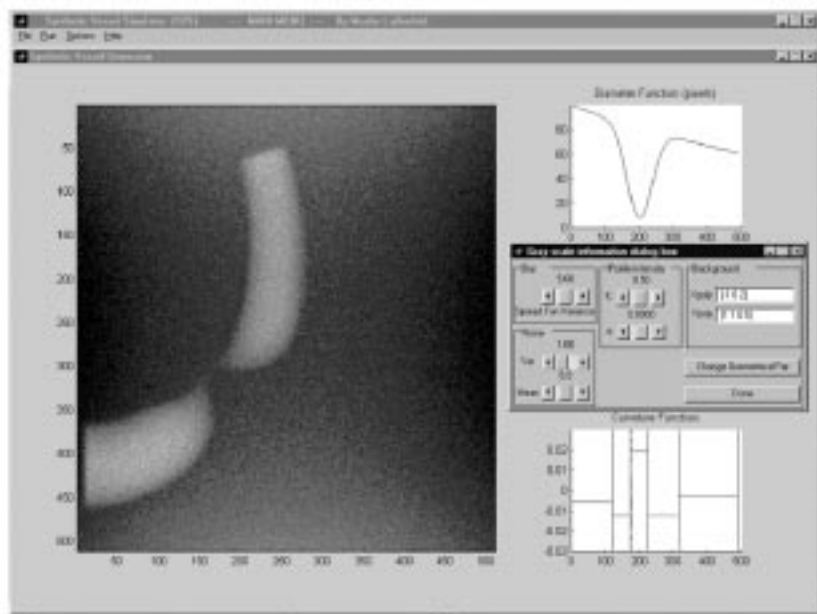
The SVG is utilized for the evaluation of centerline detection algorithms. Our goal is to derive the correspondence between an algorithm's performance and the geometrical parameters of the vessel. We implement two geometrical tracking algorithms following two well-known algorithms in the literature. One will be referred to as "Sun algorithm" based on Sun (1989) [16] and the second will be referred to as "Bolson algorithm," based on Bolson *et al.* (1980) [26]. In the following, we describe the algorithms as implemented in this work based on the cited publications.

The Sun algorithm as implemented in this work is the following iterative process (see Fig. 4).

- 1) *Initialization*: user defines initial point of centerline and initial direction.
- 2) *Estimation*: start with the current centerline point and direction, \mathbf{p}_{k-1} and \mathbf{t}_{k-1} , respectively. Estimate the next centerline point, \mathbf{p}_k^1 , by linear extrapolation of the current centerline point and its direction. New point is



(a)



(b)

Fig. 3. The synthetic vessel generator (SVG) tool. Shown is the user interface for (a) generating the 2-D geometrical model and (b) incorporating the vessel projection intensity image. The 2-D synthetic vessel is constructed of five constant curvature segments (user defined, bottom right) with a diameter function (as selected and shown upper right). The vessel projection intensity model includes a white Gaussian noise of gray level variance and a Gaussian blur of variance 5.

- found at a distance d from point \mathbf{p}_{k-1} vi a line with orientation \mathbf{t}_{k-1} . The estimated new direction \mathbf{t}_k^1 is taken as the previously found direction.
- 3) *Measurement*: draw a profile at point \mathbf{p}_k^1 perpendicular to the direction \mathbf{t}_k^1 (profile 1). Calculate the profile's midpoint, \mathbf{p}_k^2 .
 - 4) *Correction*: correct the position and the direction of the estimated centerline point. Position is updated to \mathbf{p}_k^2 ; Orientation is updated as follows: a line is drawn connecting points \mathbf{p}_{k-1} and \mathbf{p}_k^2 . A profile is drawn perpendicular to the line (profile 2).
 - 5) *Iteration*: repeat steps 3) and 4) for the corrected new centerline point.

- 6) *Tracking*: Return to step 2) to estimate the next centerline point.

In the Sun algorithm, we make the following two assumptions (these assumptions are mentioned in [16] as well): 1) For small intervals, the vessel's centerline can be estimated by a straight line; 2) The vessel's diameter function varies slowly enough to produce better correction by iterating the measurement and correction steps. The magnitude of the linear interpolation (d) used in the estimation step is taken to be proportional to the vessel's radius, R , at that point

$$d = K_r R. \quad (9)$$

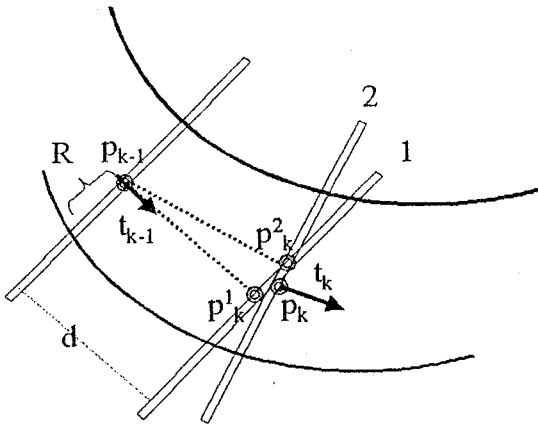


Fig. 4. Sun algorithm; Illustration of the extrapolation-update process of tracking.

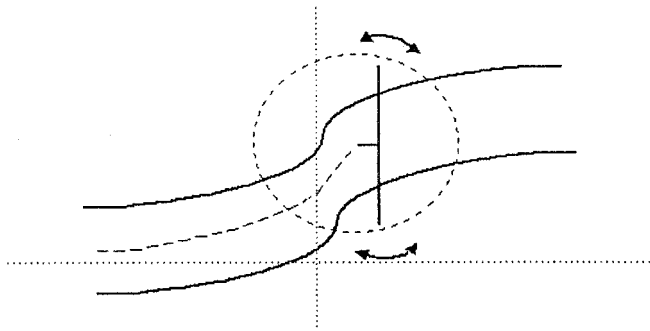


Fig. 5. Centerline calculation using a rotating T-shaped construct.

We refer to d as the *stem length*. The *stem length coefficient*, K_r , has a significant influence on the performance of the algorithm. The optimal value for K_r varies for different vessels.

The Bolson algorithm is based on the following centerline definition: the midpoint of the intersection-points of profiles drawn perpendicularly to it with the vessel borders (see Fig. 5). The user defines an initial point for the centerline and its initial direction. A new centerline point position and orientation are found using a T-shaped structure with long arms perpendicular to a short stem which is anchored at its base to the previous centerline point. The T-shape proportions are chosen as follows: the stem length is $d = K_r R$. The arms are of length $2R$ each. Note that the dimensions are adaptive to the current center point and the related radius R .

The T-shape structure is rotated and an orientation is sought in which the distances from the intersected border points, along the two T-shape arms, are equal (up to a predefined threshold). The intersection of the stem and arms of the T-shape structure is the next point of the centerline. Note that the search for the next centerline point is constrained to a certain threshold angle (\pm), from the current estimated centerline direction. The orientation threshold is used to avoid situations in which the orientation is large enough to enable backtracking in the reverse direction (i.e., algorithm decides on a previously found point as the next one).

As in the Sun algorithm, the Bolson algorithm includes an assumption that the centerline may be approximated by a straight line for small distances (relative to the magnitude of the stem

length), and that the diameter function is a slow-varying function with respect to these distances. Here, as in the Sun algorithm, the stem length parameter plays a significant role.

Both algorithms need user-defined initial conditions, for the first point of the centerline and its direction. Note the following algorithm differences: In the Sun algorithm, the next estimated point (after the correction step) can be at any distance and direction from the previous point whereas in the Bolson algorithm a constraint on the distance and orientation is introduced. This constraint may result in a more stable and accurate performance in “low dynamic” vessel scenarios, yet it may cause difficulties in coping with sudden changes in the centerline’s direction or in the magnitude of the diameter.

V. PERFORMANCE EVALUATION STUDY

We start an algorithmic evaluation study by defining a set of computational distance measures. These measures are used to evaluate and compare the Sun and Bolson algorithms, as defined herein. In this section, we describe the set of experiments conducted, along with experimental results. Results are evaluated and discussed in Section VI.

A. Objective Error Estimation Measures

A set of error estimation measures is defined between the *estimated* centerline and the *reference* centerline. In the error measurement process, an important and challenging first step is to find the correspondence between points on the two centerlines. In [13], for each point on an observer-defined centerline, the closest point on the computer-detected centerline is taken as the corresponding point. Minimal distance (or shortest path) measures are used in skeleton extraction (e.g., [23]). In this paper, we use a correspondence scheme that is based on the fact that the true centerline and the true profiles are known. We associate a point on the estimated centerline that lies on a particular profile from the reference centerline: A perpendicular line (profile) is drawn from a given selected point on the reference centerline. The intersection point of the perpendicular with the estimated centerline is used as the corresponding point of the estimated centerline. This procedure assures that the two points lie on the same curvature radius (of the reference centerline). More formally: let $r_n(\theta) = r_0 + (1/K_n)e^{j\theta}$ represent the n th segment of the reference centerline in polar coordinates, where K_n is its curvature, r_0 is its center of curvature and $\theta_0 \leq \theta \leq \theta_L$. Let $\{\hat{x}_i, \hat{y}_i\}$ denote the set of points representing the estimated centerline. Transforming the estimated centerline to a polar coordinate system centered at r_0 , results with the set $\{r_0 + r_i e^{j\theta_i}\}$ where the i th point corresponds to point $r_n(\theta_i)$ of the reference centerline ($\theta_0 \leq \theta_i \leq \theta_L$). The radial distance between the two corresponding points is $d_i = (1/K_n) - r_i$. Orientation distance between the two points, o_i , is computed, in degrees, as the difference between the corresponding tangents at the selected pair of points. B-spline interpolation is conducted prior to the distance computations.

Distance measures are computed based on the above-defined radial and orientation distances: A *normalized global distance error* is defined as: $d_{\text{NORM}} = \sqrt{(1/N) \sum_{i=1}^N (d_i^2/r_i^2)}$, where r_i is the vessel’s radius at the measured point, and N is the number of points used for the distance error calculations. The

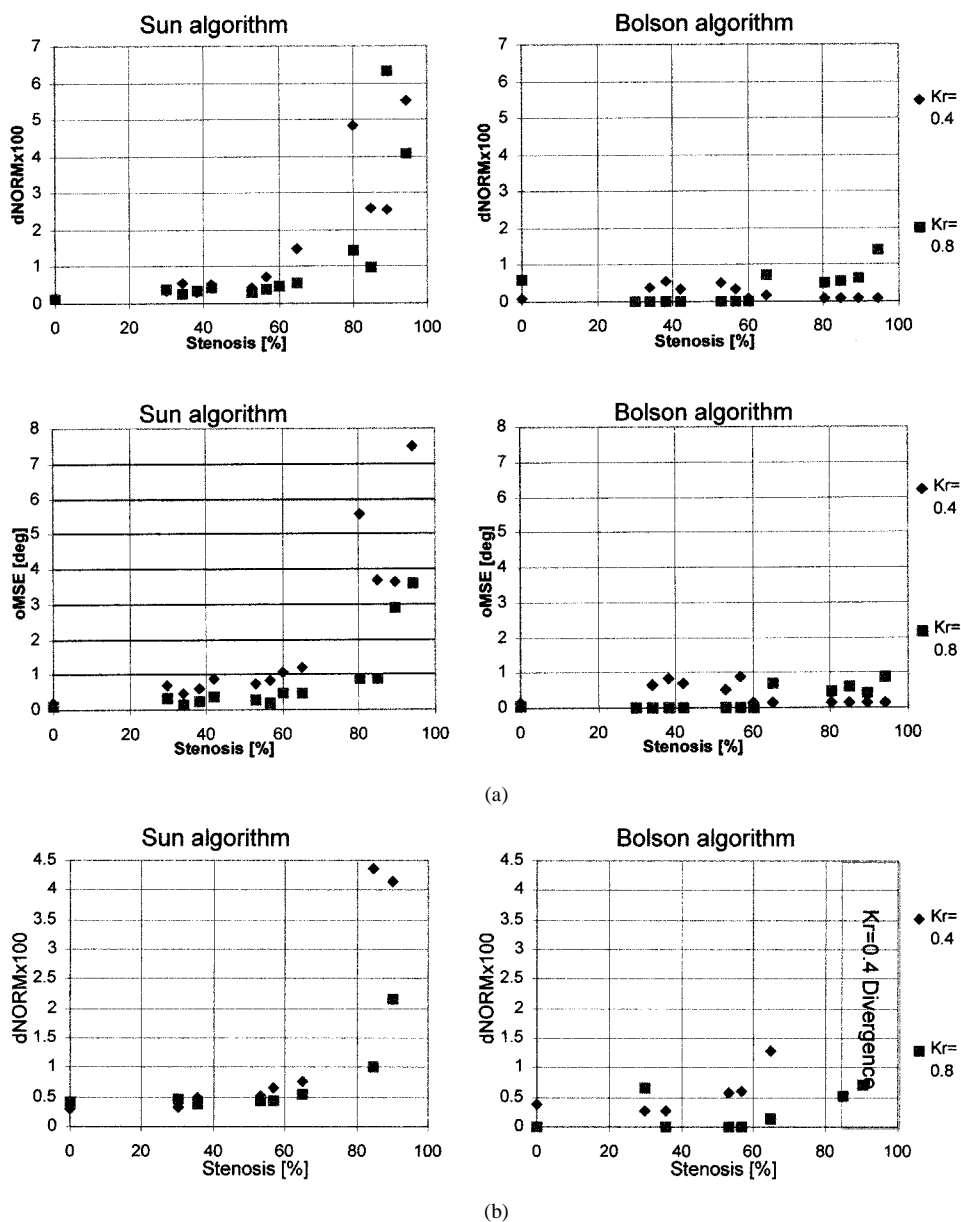


Fig. 6. (a) Zero taper, no curvature. Results for the Sun and Bolson algorithms for different stenosis values (vessels #1–#12). Distance error and orientation error are plotted, top and bottom, respectively. (b) Medium taper vessels $a = -0.00145$ no curvature. Results for the Sun and Bolson algorithms for different stenosis values (vessels #13–#19). Distance error is shown. Similar results are received with the orientation error measure.

normalized distance takes into account the fact that the distance between centerlines near a stenosis, where the vessel’s diameter is small, should be considered more significant than at vicinities where the vessel’s diameter is large. A *global orientation performance measure* is defined as the mean square error (OMSE): $O_{MSE} = \sqrt{(1/N) \sum_{i=1}^N O_i^2}$, where O_i is the orientation error measured in degrees at the i th point. In some experiments, a normalized version of the orientation measure is used: $O_{NORM} = 1/K_j \sqrt{(1/N) \sum_{i=1}^N O_i^2}$ where K_j is the vessel’s j th segment curvature.

B. Algorithm Parameters

Several parameters need to be defined in the implementation of the Sun and Bolson algorithms. In the Bolson algorithm, we use two parameters: 1) Kr , which is the magnitude constant of the stem length and 2) the total search angle. The Kr parameter

is also used in the Sun algorithm. Taking into account the significance of the Kr parameter (as discussed earlier) two values for Kr were chosen (0.4 and 0.8) with which all the runs were performed. The results will be dually presented. The additional Bolson algorithm parameter, total search angle, is kept constant at $\pm 30^\circ$.

The distance error is measured in pixels and the orientation errors in degrees. A divergence is defined as a case in which the algorithm fails to track more than 60% of the vessel segment’s length. Initial conditions, such as starting point position and orientation deviations, were set to zero.

C. Experimental Results

In the following, we present a sample of experimental runs. A correspondence between the algorithms’ performance and the simulated vessel geometrical parameters is experimentally

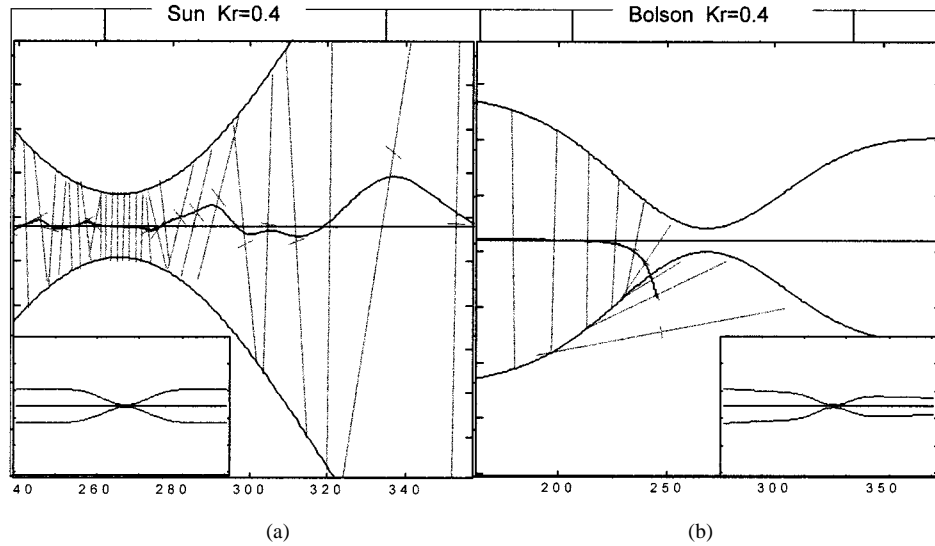


Fig. 7. A zoom-in view of a nontapered image (#12), (a) Sun algorithm, and medium tapered image (#19), (b) Bolson algorithm with $Kr = 0.4$. The reference centerline and the interpolated estimated centerline are displayed. The profiles are the estimated profiles (algorithm output, with no smoothing applied) and their mid points are the (nonsmoothed) estimated centerline points. The estimated centerline shown is the result of interpolating (B-spline) across the shown centerline points. The corresponding vessel images are displayed in the lower corners.

sought. We, therefore, focus on cases in which some errors are present, i.e., deviations between the estimated and reference centerlines are found.

We start with the case of a *constant taper* value and differing levels of stenosis. The vessel is constructed of a single zero curvature segment. Two different taper values (parameter α) are used: 0 and 0.00145, while altering the stenosis parameter [Table I(a) and Fig. 12(a)]. The stenotic region is in the middle of the vessel's arc-length. Fig. 6(a) and (b) present the results for the two taper cases. In Fig. 6(a), 13 errors are plotted, for each one of 13 vessels [vessel numbers #1–#12 in Table I(a), along with a vessel with zero stenosis]. In Fig. 6(b), eight error samples are plotted (corresponding to vessels #13–#19, along with a zero-stenosis vessel). In zero-taper vessels, the Bolson algorithm performance errors are of small magnitude and are almost indifferent to the stenosis parameter, while the Sun algorithm performance is exponentially related to the stenosis parameter. In the 0.00145 taper vessels, both algorithms' performance shows an exponential type of behavior as a function of the stenosis parameter. Both algorithms show better results with $Kr = 0.8$. For $Kr = 0.4$, the Sun algorithm may result in a sinusoidal (jittery) behavior in the stenosis region, as shown in Fig. 7(a). In Fig. 7(b), we see a sample run with $Kr = 0.4$ and stenosis over 70% in which the Bolson algorithm results in divergence.

Figs. 8 and 9 show example runs of *Curved vessel (knee-type) scenarios* [corresponding vessels are shown in Table I(b) and Fig. 12(b)]. The graphs of Fig. 8 present the Log of the performance error as a function of the curved segment arclength (θ) and curvature (K). Both algorithms show a clear exponential relationship between the performance and the curvature (linear in the Log scale). The Sun algorithm diverges for arc-lengths larger than 0.92 radians (all curvature values). The Bolson algorithm shows a performance decreasing in a linear manner with curvature. Fig. 9 shows an example run for the Sun and Bolson algorithm in curved vessels.

The final set of experimental results is shown in Figs. 10 and 11 for the case of *Curved vessels with Stenosis*. In this vessel group, the vessels combine constant taper with variable stenosis, curvature and arclength [Table I(c) and Fig. 12(c)]. The images are divided into three categories, in each one the vessel's curvature and arclength are kept constant: Class I: curvature = 0.003, arclength = 0.94 rad. Class II: curvature = 0.0089, arclength = 1.25 rad. Class III: curvature = 0.015, arclength = 1.57 rad. In Fig. 10(a), the case of $Kr = 0.4$ is shown. Sun algorithm performance shows an exponential behavior as a function of the stenosis, with a constant increase between the vessel categories. The Bolson algorithm exhibits divergence in all curvature classes at the high stenosis range (around 90%), and divergence at the higher curvature cases (class III) at stenosis levels as low as 50%. An increase in the Kr parameter value improves the algorithm's ability to cope with such vessels. This is shown in Fig. 10(b). With $Kr = 0.8$, the Sun algorithm performance changes as well. Divergence occurs at low stenosis for high curvature and arc-length vessels (class III). A set of sample runs is shown in Fig. 11. For $Kr = 0.8$, both algorithms perform well. For $Kr = 0.4$, Sun algorithm shows a jittery behavior. The Bolson algorithm fails to track the vessel's centerline.

VI. DISCUSSION

A main objective of this work is to present the concept of benchmarking in QCA algorithms, using objective measures and tools such as the synthetic vessel generation tool (SVG). It is not our goal to provide a complete analysis of a particular algorithm. Running experiments such as the ones presented enables a more complete understanding of a given algorithm's sensitivity to geometrical parameters of the vessel, and also enables tuning the algorithm's parameters and comparing across algorithms. In order to investigate correspondence between vessel geometry and algorithm performance, we implemented centerline extraction algorithms that are based on two well-known algorithms in the literature. The reference algorithms of Sun [16]

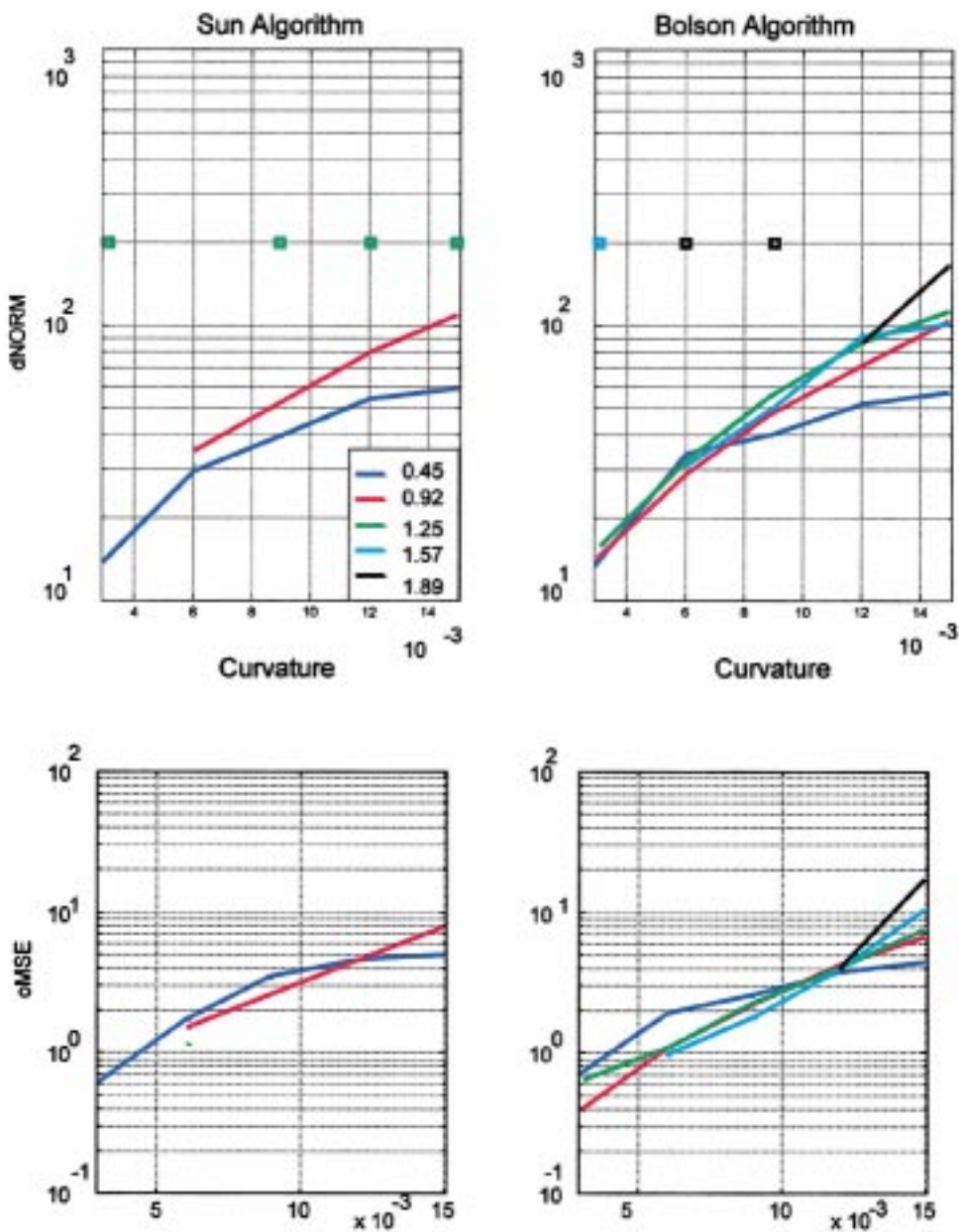


Fig. 8. Highly curved vessels. Sun and Bolson algorithms’ performances for $Kr = 0.8$ as a function of vessel’s second segment curvature for different values of arc-length (vessels #20–#43). The arc-length is measured in radians and its values presented in the legend. $oMSE$ is measured in degrees and d_{NORM} is multiplied by 1000. Divergence is displayed as empty squares at the appropriate curvature value, if divergence occurred for all curvature values the divergence squares are not displayed.

and Bolson [26] are efficient algorithms that are the basis of many successful QCA systems. The results we present should be considered in reference to the particular implementation of the algorithms herein, as outlined in Section IV, as well as to the particular set of objective measures, as outlined in Section V.

An interesting set of observations and conclusions may be extracted from the experiments in Section V. In Fig. 6(a) and (b), we see that the Bolson algorithm is sensitive to the vessel’s taper value, as well as to the added stenosis, while the Sun algorithm is sensitive to the stenosis, regardless of the taper diameter change. Fig. 7 demonstrates that for small Kr the Sun algorithm may result in a sinusoidal (jittery) behavior in the stenosis region. We associate the deviation of the estimated centerline from

the reference centerline, in this ideal straight centerline case, to quantization errors (pixel resolution) introduced in the synthetic image generation process. In the Sun algorithm, small deviations in the estimated point’s position can be translated to large deviations in orientation due to the small stem length. Fig. 7 (right) shows a sample run with $Kr = 0.4$ and stenosis over 70% in which the Bolson algorithm does not handle the rapid changes of the vessel’s diameter function and results in divergence. In this case, small deviations from the reference centerline build up and cause divergence in the stenosis vicinity. From the set of experiments shown in Figs. 8 and 9 we conclude that the Sun algorithm has difficulty in coping with highly curved, long arc-length segments. The arc-length parameter has a strong

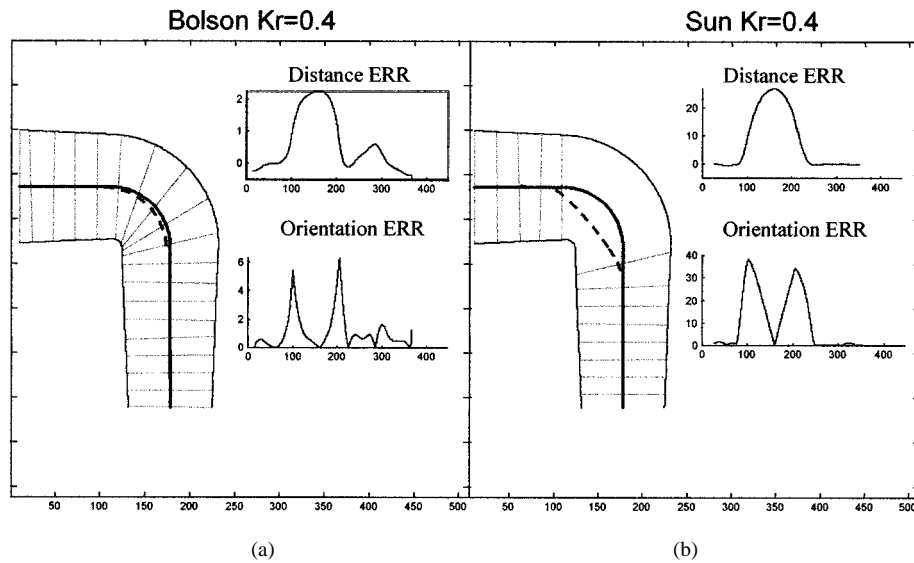


Fig. 9. (a) Bolson and (b) Sun results with $Kr = 0.4$ in a knee-type vessel (#25). The reference centerline and the interpolated estimated centerline are displayed as solid and dashed lines, respectively. The gray profiles are the nonfiltered estimated profiles and the mid points are the nonfiltered estimated centerline points. In the small graphs, the distance and absolute orientation errors are displayed as a function of the reference centerline arc-length. Sun shows difficulty in coping with highly curved segment, divergence occurs when applied with $Kr = 0.8$.

impact on the performance of the algorithm, with more severe response at larger Kr . The Bolson algorithm seems to be more robust to arc-length changes, with performance decreasing in a linear manner with curvature.

An analysis of cases in which a stenosis is added to the curved vessels is presented in Figs. 10 and 11. In the case of $Kr = 0.4$ [see Fig. 10(a)], the Sun algorithm performance shows an exponential behavior as a function of the stenosis, with a constant increase between the vessel categories. The Bolson algorithm shows inferior results, with divergence in all curvature classes at the high stenosis range (around 90%), and divergence at the higher curvature cases (class III) at stenosis levels as low as 50%. The results of the Bolson algorithm may be explained by its lack of an orientation continuity constraint and thus its failure to cope with rapidly changing diameter vessels. An increase in the Kr parameter value improves the algorithm's ability to cope with such vessels. This is shown in Fig. 10(b), with $Kr = 0.8$. The Sun algorithm performance changes with the increase in Kr as well. Here we see that divergence occurs at low stenosis for high curvature and arc-length vessels (class III). A possible explanation for the fact that no divergence was experienced at larger stenosis is that a stenosis introduced on top of the curved vessel effectively reduces the Kr parameter at the stenosis region, effectively bringing us back to the smaller Kr scenario.

From the set of experiments conducted, we may conclude that the set of synthetic vessels can be divided into two major groups, one corresponding to *highly curved vessels* and the other to *rapidly changing diameter vessels*. Although limited in scope, the results may be summarized to indicate that the Bolson algorithm performs well in curved vessel scenarios while the Sun algorithm copes well when applied to high-gradient diameter functions. The Bolson algorithm has difficulties in coping with vessels with a rapidly changing diameter and, therefore, the dominant parameter is the vessel's stenosis, especially for small Kr values. Using a stem that is too short results in difficulties

to find the next centerline point in a rapidly changing diameter function (e.g., near a stenosis). Using a stem that is too big results in difficulties in tracking a highly curved centerline. The Sun algorithm is more sensitive to highly curved segments; thus the dominant parameter is the vessel curvature and arc-length for large values of Kr .

An increase in centerline estimation error is seen with the addition of curvature into the vessel. Comparing Figs. 6 with 10, we note that in the Sun algorithm, there is a stronger increase in error with increase in stenosis. For example, at the 90% range with $Kr = 0.8$, the Sun algorithm shows an error of 100–200 pixels [see Fig. 6(b)] while an error of 400 pixels is present with curvature added [see Fig. 10(b)]. In the Bolson algorithm, introducing additional curvature resulted in the divergence occurring at lower stenosis percentile. With no curvature and $Kr = 0.4$, divergence occurs at 90% stenosis [see Fig. 6(b)] while with the added curvature divergence occurs already at the 50% stenosis range [see Fig. 10(a)]. These results indicate that a given QCA algorithm's performance does in fact depend on the vessel geometry.

The experiments presented were performed on a small set of data thus the results need to be considered with care. Position and orientation errors are used throughout. Although we expect that the orientation information is important, in this set of experiments there was no clear distinction between the two. Initial experimentation of asymmetric vessels [Table I(d) and Fig. 12(d)] did not exhibit any differences in the results.

VII. CONCLUSION

We presented a simulation tool (SVG) for generating synthetic vessel angiographic images under predetermined geometrical parameters. A method for calculating global performance measures based on the comparison of the reference centerline and an estimated centerline was implemented. The simulation

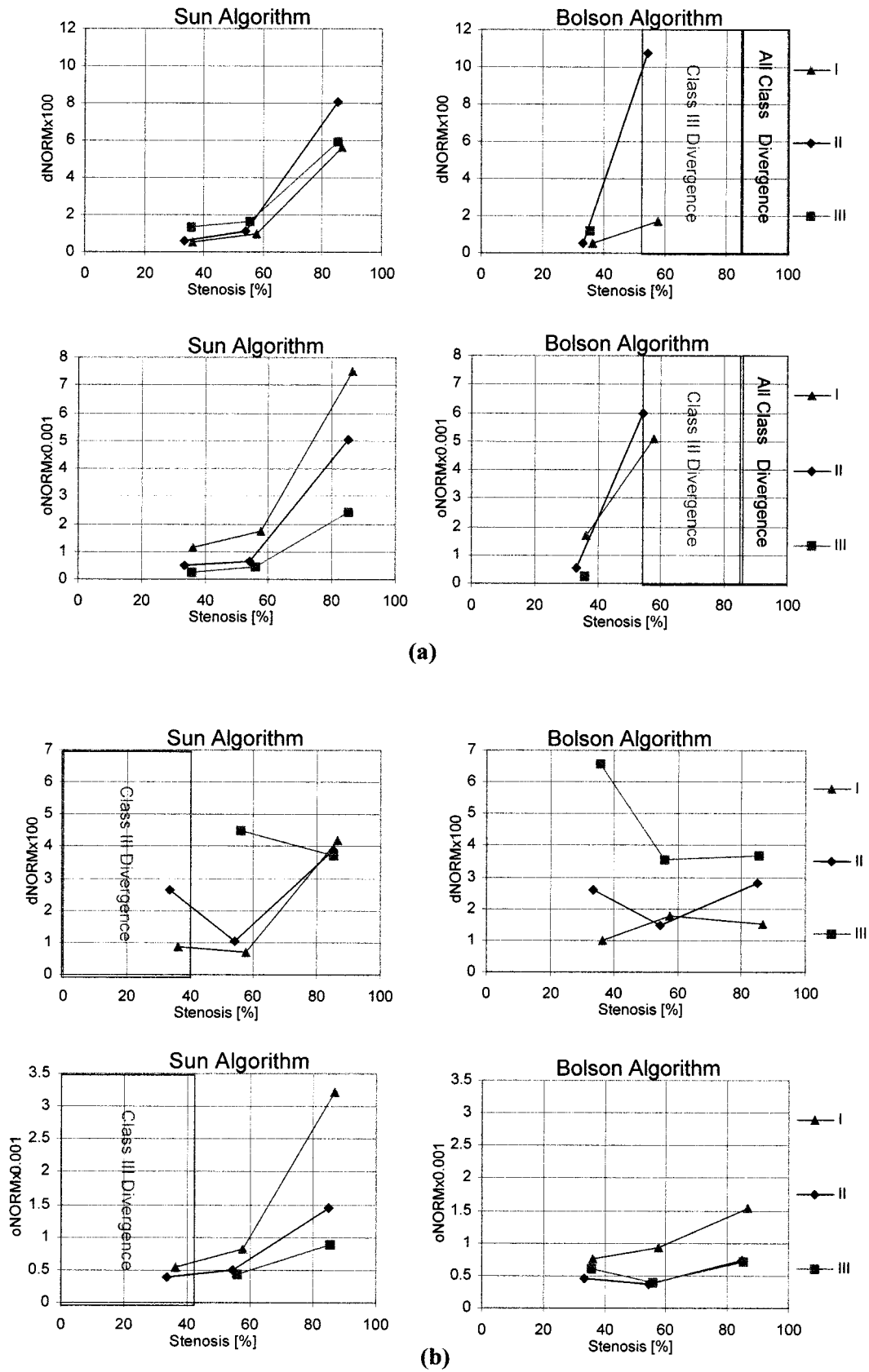


Fig. 10. Sun and Bolson algorithms' performances for (a) $Kr = 0.4$ and (b) $Kr = 0.8$ as a function of stenosis in three classes of knee type vessels. Class I: curvature = 0.003, arclength = 0.94 rad (vessels #44–#46). Class II: curvature = 0.0089, arclength = 1.25 rad (vessels #47–#49). Class III: curvature = 0.015, arclength = 1.57 rad (vessels #50–#52).

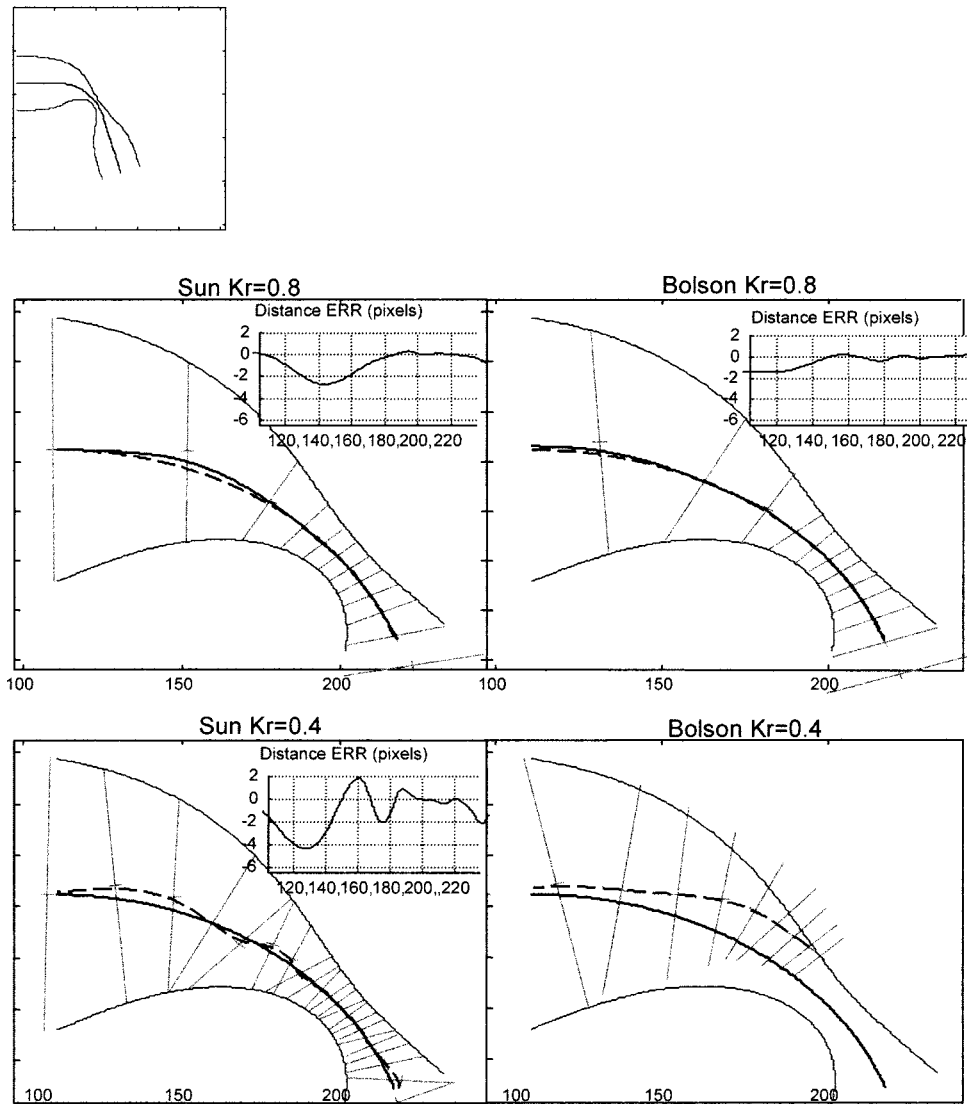


Fig. 11. Sun and Bolson example run results for the second segment of image #49 (shown on top). The reference centerline and the interpolated estimated centerline are displayed as solid and dashed lines, respectively. The profiles are the nonfiltered estimated profiles and their mid points are the nonfiltered estimated centerline points. In the small graphs, the distance error is displayed as a function of the reference centerline arc-length.

tool enables an objective comparison between algorithms and a means of understanding the relation between the algorithms' performances and the geometrical parameters of the vessel.

The paper, in its current version, is more of a concept-presentation. First, we raise the possibility and need for benchmarking QCA algorithms, such as centerline extraction algorithms. We present a first step in this direction, in which we introduce the idea of a synthetic vessel generation (SVG) and study tool, and demonstrate several of its capabilities with a couple of classical well-known algorithms from the literature. A second concept we present in the paper is the idea of the dependence of QCA performance on vessel geometry. We believe this issue has not been addressed in the literature, and we are able to demonstrate its importance with the SVG tool and the two algorithms chosen.

In the performance evaluation procedure, it may be of interest to use additional distance measures to the ones proposed in this paper, as well as different means of determining correspondence between the estimated and the reference centerlines

(such as minimal distance correspondence). Once selected and consistently applied in the evaluation study, the sensitivity of the different algorithms to vessel geometry can be analyzed and compared. In future work, we plan to focus on a more exhaustive performance evaluation study, using the concepts thus presented. A comparison is needed between additional and more updated centerline extraction algorithms available in the literature. Using the SVG tool, sensitivities of existing algorithms can be learned, leading to the possibility of developing updated centerline extraction algorithms.

A current limitation of the SVG tool is that there is no automatic means to prevent the generation of extreme geometrical conditions, such as vessel self-intersection. In the current version of the SVG system, this issue is the responsibility of the user. The vessel generation process is interactive and the user may update the parameters to generate desired vessel geometry. Including predefined parameter ranges to ensure no self-intersection is a desired feature of the system. We are currently ex-

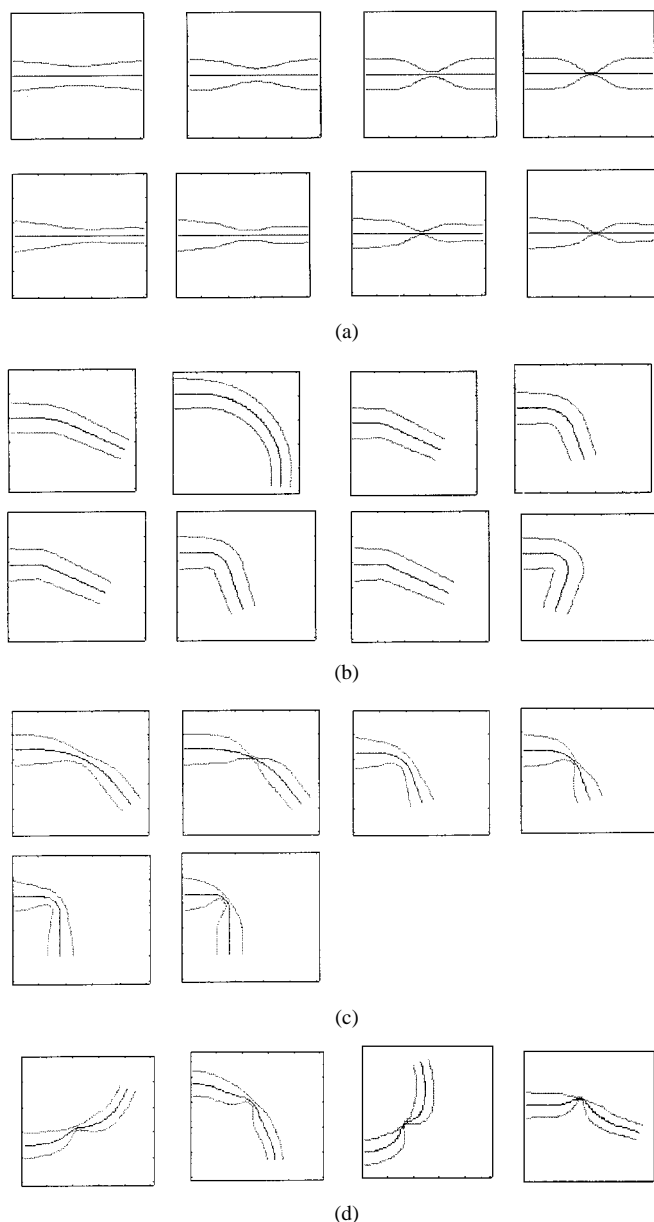


Fig. 12. Sample vessel images. (a) A set of vessels with zero curvature; zero taper or medium taper value; with stenosis. In the top row are shown zero taper vessels no. 3, 6, 10, 12, left to right, respectively. In the bottom row, medium taper vessels no. 14, 16, 17, 19, left to right, respectively. (b) A set of vessels with varying curvature (knee-type); no stenosis. Shown are vessels no. 20, 23, 29, 31, left to right, respectively; Bottom row, no. 34, 36, 39, 43. (c) A set of vessels with curvature; with stenosis. Shown are vessels no. 45, 46, 48, 49, 51, 52 left to right, top to bottom, respectively. (d) A variety of additional vessels, including multiple-segment vessels and asymmetric stenosis vessels. Shown are vessels no. 54, 55, 59, 61.

tending the SVG to include stenosis computations and intensity profiling. Important future work includes the consideration of real angiographic data. The challenge is to extract an appropriate geometric model from a given angiographic image and specifically, to extract a geometrical description of the vessel centerline that can be analyzed with the SVG tool.

REFERENCES

- [1] L. M. Zir, S. W. Miller, R. E. Dinsmore, J. P. Gilbert, and J. W. Harthorne, "Interobserver variability in coronary angiography," *Circ.*, vol. 53, no. 4, pp. 627–676, 1976.
- [2] C. W. White, C. B. Wright, D. B. Doty, L. Hiratzka, C. L. Eastham, D. G. Harrison, and M. L. Marcus, "Does visual interpolation of the coronary arteriogram predict the physiologic importance of coronary stenosis?," *N. Eng. J. Med.*, vol. 310, pp. 819–824, 1984.
- [3] T. Sandor, A. D'adamo, W. B. Hanlon, and J. R. Spears, "High precision quantitative angiography," *IEEE Trans. Med. Imag.*, vol. MI-6, pp. 258–265, Sept. 1987.
- [4] J. H. C. Reiber, P. W. Serruys, and J. D. Barth, "Quantitative coronary angiography," in *Cardiac Imaging*, M. L. Marcus, H. R. Schelbert, D. J. Skorton, and G. L. Wolf, Eds. Philadelphia, PA: Saunders, 1991, pp. 211–280.
- [5] J. H. C. Reiber *et al.*, "Coronary artery dimensions from cineangiograms- methodology and validation of a computer-assisted analysis procedure," *IEEE Trans. Med. Imag.*, vol. MI-3, pp. 131–141, Sept. 1984.
- [6] M. T. Le Free *et al.*, "Digital angiographic assessment of coronary arterial geometric diameter and videodensitometric cross-sectional area," *Proc. SPIE*, vol. 626, pp. 334–341, 1986.
- [7] S. R. Fleagle *et al.*, "Automated analysis of coronary arterial morphology in cineangiograms: Geometric and physiological validation in humans," *IEEE Trans. Med. Imag.*, vol. 8, pp. 387–400, 1989.
- [8] A. K. Klein, F. Lee, and A. A. Amini, "Quantitative coronary angiography with deformable spline models," *IEEE Trans. Med. Imag.*, vol. 16, pp. 468–482, Oct. 1997.
- [9] Y. Sato, T. Araki, M. Hanayama, H. Naito, and S. Tamura, "A viewpoint determination system for stenosis diagnosis and quantification in coronary angiographic image acquisition," *IEEE Trans. Med. Imag.*, vol. 17, pp. 121–137, Feb. 1998.
- [10] C. Seiler, R. L. Kirkeeide, and K. L. Gould, "Basic structure-function relations of the epicardial coronary vascular tree," *Circulation*, vol. 85, pp. 1987–2003, 1991.
- [11] M. Garreau, J. L. Coatrieux, R. Collorec, and C. Chardenon, "A knowledge-based approach for 3-D reconstruction and labeling of vascular networks from biplane angiographic projections," *IEEE Trans. Med. Imag.*, vol. 10, pp. 122–131, June 1991.
- [12] T. Saito, M. Misaki, K. Shirato, and T. Takishima, "Three-dimensional quantitative coronary angiography," *IEEE Trans. Biomed. Eng.*, vol. 37, pp. 768–777, Aug. 1990.
- [13] T. N. Pappas and J. S. Lim, "A new method for estimation of coronary artery dimensions in angiograms," *IEEE Trans. Acoust., Speech, Signal Processing*, vol. 36, no. 9, pp. 1501–1513, Sept. 1988.
- [14] M. Sonka, M. D. Winniford, and S. M. Collins, "Robust simultaneous detection of coronary borders in complex images," *IEEE Trans. Med. Imag.*, vol. 14, pp. 151–161, Mar. 1995.
- [15] K. L. Parker, K. L. Pope, R. van Bree, and H. W. Marshall, "Three-dimensional reconstruction of moving arterial beds from digital subtraction angiography," *Comput. Biomed. Res.*, vol. 20, pp. 166–185, 1987.
- [16] Y. Sun, "Automated identification of vessel contours in coronary arteriograms by an adaptive tracking algorithm," *IEEE Trans. Med. Imag.*, vol. 8, pp. 78–88, Mar. 1989.
- [17] K. Kitamura, J. B. Tobis, and J. Sklansky, "Estimating the 3-D skeletons and transverse areas of coronary arteries from biplane angiograms," *IEEE Trans. Med. Imag.*, vol. 7, pp. 173–187, 1988.
- [18] J. L. Coatrieux, J. Rong, and R. Collorec, "A framework for automatic analysis of the dynamic behavior of coronary angiograms," *Int. J. Cardiac Imag.*, vol. 8, pp. 1–10, 1992.
- [19] I. Liu and Y. Sun, "Recursive tracking of vascular networks in angiograms based on detection-deletion scheme," *IEEE Trans. Med. Imag.*, vol. 12, pp. 334–341, 1993.
- [20] K. Haris *et al.*, "Model-based morphological segmentation and labeling of coronary angiograms," *IEEE Trans. Med. Imag.*, vol. 18, pp. 1003–1015, Oct. 1999.
- [21] Y. Zhou and A. W. Toga, "Efficient skeletonization of volumetric objects," *IEEE Trans. Visual. Comput. Graphics*, vol. 5, pp. 196–209, July/Sept. 1999.
- [22] Y. Zhou, A. Kaufman, and A. W. Toga, "3D skeleton and centerline generation based on approximate minimum distance field," *Visual Comput.*, vol. 14, no. 7, pp. 303–314, 1998.
- [23] M. Sonka, M. D. Winniford, X. Zhang, and S. M. Collins, "Lumen centerline detection in complex coronary angiograms," *IEEE Trans. Biomed. Eng.*, vol. 41, pp. 520–528, June 1994.
- [24] D. E. Rutherford, *Vector Methods*. New York: Wiley Interscience, 1959.
- [25] A. K. Jain, *Fundamentals of Digital Image Processing*. Englewood Cliffs, NJ: Prentice-Hall, 1989.
- [26] E. L. Bolson, S. Kliman, F. Sheehan, and H. T. Dodge, "Left ventricular segmental wall motion analysis -a new method using local direction information," presented at the Proc. Computers in Cardiology, Piscataway, NJ, 1980.